Pergamon

0301-9322(94)00054-9

Int. J. Multiphase Flow Vol. 21, No. 1, pp. 1–26, 1995
Elsevier Science Ltd. Printed in Great Britain

DYNAMICS OF FLUIDIZED SUSPENSIONS OF SPHERES OF FINITE SIZE

P. SINGH and D. D. JOSEPH

Department of Aerospace Engineering and Mechanics, University of Minnesota, Minneapolis, MN 55455, U.S.A.

(Received 15 January 1993; in revised form 12 June 1994)

Abstract—We propose a one-dimensional theory of fluidized suspensions in which the fluids and solids momentum equations are decoupled by using a new mean drag law for the particles. Our mean drag law differs from the standard drag laws frequently used in that the drag is assumed to depend on the area fraction rather than the number density. For a monodisperse suspension of spheres of radius R, the area fraction and the number density are related by a simple geometrical construction that takes into account the area of intersection of the spheres with a plane perpendicular to the flow. For the linearized theory uniformly fluidized suspension is unstable but not Hadamard unstable. However, there is a distinguished set of marginally stable modes belonging to a countable set of blocked wave numbers α: $\alpha = 4.493/R$, $7.7253/R$, $10.904/R, \ldots$ The nonlinear theory contains bounded solutions when a certain dimensionless "growth rate" parameter is below a critical value. The power spectrum of these bounded solutions is broad banded in both space and time, and is very low for the wave numbers that are marginally stable in the linear theory. These results agree with our experiments, as well as with the previous experimental results from diffraction studies.

Key Words: fluidized suspensions, radial and area-averaged distributions, particle phase theories, Hodamard instability, bubbling instability, bounded solutions

1. INTRODUCTION

We begin with a brief description of the nature of voidage fluctuations in fluidized suspensions as observed by various authors. We first discuss the experiments done in two-dimensional beds and then similar experiments done in three-dimensional beds. Photographs of the motion of solid spherical particles fluidized by water in our two-dimensional bed (see figure 1) are shown in figure 2.

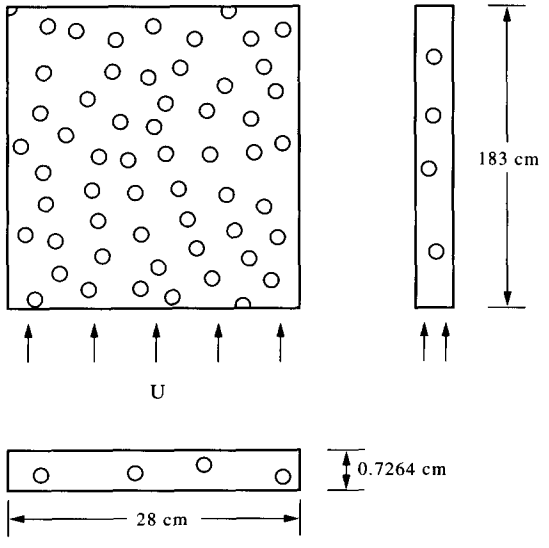

Figure 1. Schematic diagram of the two-dimensional bed used to carry out experiments. Particle diameters are listed in table 1. The bed is actually three-dimensional but the particles are constrained to move in two dimensions.

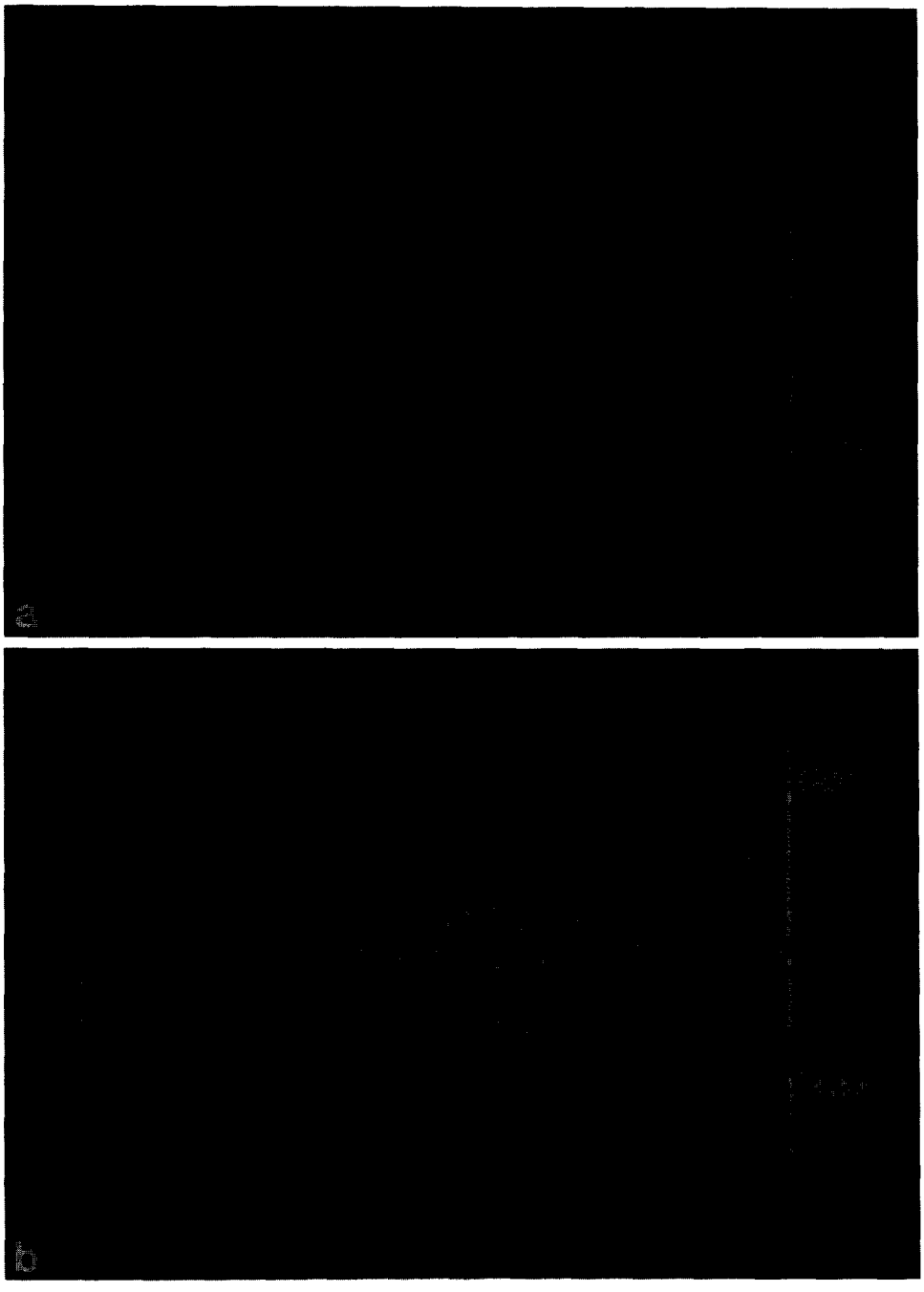

Figure 2. Re = 300. The spatial distribution of particles is nonuniform.

Beds of particles confined to move in two dimensions have been studied before by Volpicelli *et al.* (1966); Garside & Al-Dibouni (1973); Joseph *et al.* (1987); Fortes *et al.* (1987); and Singh *et al.* (1989). We refer to these as VMZ, GA, JFLS, FJL and SCFJL. More photographs of fluidization in two-dimensional beds can be found in these papers and Singh (1991). VMZ showed that when the particles are in a fluidized state, i.e. void fraction $\epsilon > 0.45$, the fluidized bed correlations of Richardson & Zaki (1954) are also satisfied in a two-dimensional bed. In particular, they obtained a correlation relating the composite or superficial velocity u_c to the void fraction, ϵ, $u_c = V\epsilon^n$, where n depends on Reynolds number as in the Richardson & Zaki correlation and V is the free fall velocity of a single particle. This and other observations of VMZ are in good agreement with our observations (see Singh 1991). Furthermore, when the fluidizing velocity is only slightly greater than the minimum needed for fluidization, many spheres are aggregated and the beds exhibits

voidage cracks which propagate by particles dropping out of the roof (see JFLS, FJL). At higher fluidizing velocities, on the other hand, the bed spreads much more uniformly and the neighboring particles move independently on paths that are quasi-random. In this regime, the fluctuations of the particle velocities and the number density are also quasi-random.

Even though the particle trajectories in three-dimensional beds appear to be qualitatively similar, the above quantitative visual observations can be made relatively easily only for two-dimensional beds. For three-dimensional beds, however, it is easier to use the diffraction techniques to obtain the spatial arrangement of the particles directly in terms of the power spectrums (also called the structure factors), i.e. the square magnitude of the Fourier transform of the number density. For example, Pusey (1978) used dynamic light scattering to measure the structure factor for a monodisperse suspension of spherical particles of 0.09 μm dia. This particular value of the particle diameter was used because the light scattering technique can be used only to probe wavelengths that are comparable to the wave length of the visible spectrum. Wai *et al.* (1987); Wignall *et al.* (1990) and Ottewill (1991), on the other hand, have used neutron scattering to obtain the structure factor for 0.1 μm uniform spheres, i.e. spheres that have the scattering density uniformly distributed within the particles; as well as for 0.1 μm spheres that have a neutron transparent shell and a neutron scattering core. A comparison of these experimental results with our results reported in section 5 suggests that the spatial power spectrum, and hence also the spatial arrangement of the particles for two- and three-dimensional beds, including the effects associated with wave number blockage, are similar [see section 3; Singh (1991), and Singh & Joseph (1990, 1991)].

In section 3 we consider a one-dimensional theory of fluidized suspensions in which the fluids and solids equations are decoupled, and the system is closed with a momentum equation for the particles alone. The simplest theory based on the mean drag acting on a typical particle of the fluidized suspension is used (see Jackson 1963) except that the force that the fluid exerts on the particles is assumed to depend on the **local area fraction** rather than the local number density (or equivalently the local volume fraction, when the local volume fraction is **defined** to be the product of the local number density and the volume of one particle). In a monodisperse suspension of spheres of radius R, the area fraction and the number density are related by a simple geometrical construction that takes into account the area of intersection of the spheres with a plane perpendicular to the flow, even when their centers are not exactly on the plane (see section 3 for details). Our one-dimensional theory then has three unknowns, the number density, the area fraction and the particle velocity, rather than two. The term based on the gradient of the volume fraction which expresses the particle phase pressure is not included in the present analysis. The two-variable theory is recovered in the limit $R \to 0$ or when the wavelength of the disturbance studied is much larger than R. The three-variable theory, however, is fundamentally different from the two-variable theory because for the linearized three-variable theory the uniform fluidized-suspension is not Hadamard unstable. The uniformly fluidized state is linearly unstable even in the three-variable theory, but there is a distinguished set of marginally stable modes belonging to a countable set of blocked wave numbers generated by the relation between the number density and the area fraction (see section 3).

The initial value problems for the nonlinear three-variable theory are solved numerically in a periodic domain (see section 4 for details). The solutions are bounded when a certain dimensionless "growth rate" parameter is below a critical value. These **bounded solutions** are found to be independent of the initial conditions. However, when the "growth rate" parameter is larger than the critical value then the numerical solutions are unstable in the sense that the power contained in the fluctuations grows with time, without bound. For a bounded solution, when it exists, both the temporal and the spatial power spectrums are **broad banded**, but the power level is very low for the wave numbers in the blocked set which, as we have already noted, are marginally stable in the linear theory. These results are in good agreement with the experimental results reported in section 5, and also with the results obtained by Wai, Wignall *et al.* and Ottewill for the number density distributions.

In section 5 we will report our results for the spatial distribution of the area fraction as a function of time that are obtained by analyzing the digitized video recordings of two-dimensional fluidized beds. This data is then used to obtain the temporal autocorrelation and spectrum at a point, the spatial autocorrelation and spectrum at a fixed time, as well as the two-dimensional spectrum in space and time. The temporal autocorrelation decays monotonically to zero at all Reynolds

numbers. The spatial autocorrelation, on the other hand, becomes negative and then goes to zero for large spatial shifts. The Fourier transform of the spatial autocorrelation function (i.e. the structure factor), as suggested by the geometric relation between the number density and the area fraction, contains deep minima at the blocked wave numbers (see section 3). We will show later that these minima in the Fourier transform of the spatial autocorrelation of the area fraction arise because the fluidized bed contains discrete spherical particles. The number density distribution can be obtained from the area fraction by inverting the convolution that relates the number density to the area fraction. However, since the zeros associated with the convolution function introduce error in the inversion of the convolution, an independent method is needed to verify the results of deconvolution. This verification is accomplished by using the results of the neutron diffraction studies that give the spatial Fourier transform of the number density distribution of a fluidized suspension of particles directly when the diffraction radius of the particles is different from their mechanical radius. These experiments conclusively prove that the minima of the number density and of the area fraction are at the same set of blocked wave numbers (see Wai, Wignall *et al.* and Ottewill). Obviously, the minima of the number density distribution are created by a dynamical mechanism which at present is not fully understood.

2. RADIALLY SYMMETRIC DISTRIBUTIONS

As indicated in the previous section, the results of diffraction techniques, e.g. the light and neutron scattering techniques, also show that the set of dimensionless minima of the spatial number density spectrum for a fluidized suspension is the same as the set of zeros of the blockage function (see Wai, Wignall *et al.* and Ottewill). In their analysis, however, these latter authors have used the radially symmetric distributions, to describe their results, instead of the area averaged distributions we use in this paper. But, it is easy to show that the Fourier transform of a radially symmetric distribution, and that of an area averaged distribution obtained from a radially symmetric distribution, are the same. This proves that the two distributions are equivalent from a mathematical point of view, i.e. the same information is contained in both distributions.

The radial distribution functions are used in statistical mechanics to describe the spatial distribution of atoms or molecules in liquids. Given a particle at the origin of the coordinate system, the radial distribution $g(\mathbf{r}, t)$, gives the probability of finding another particle at distance $\mathbf{r}$ from the origin. Since for isotropic systems, the radial distribution function is independent of the orientation, we have

$$g(\mathbf{r}, t) = g(|\mathbf{r}|, t).$$

In the Fourier transform space this implies that

$$g(\boldsymbol{\alpha}, t) = g(|\alpha|, t),$$

where $g(\alpha, t)$ is the Fourier transform of $g(\mathbf{r}, t)$. It is obvious that a radially symmetric distribution function can be described completely by its distribution along any one ray originating from the origin. So we need to know only, say $g(z\mathbf{k}, t)$ in the real space and $g(\alpha_z \mathbf{k}, t)$ in the Fourier transform space, where $\mathbf{k}$ is the unit vector along the z-direction and α_z is the component of α along the z-direction. Next, we show that for any radially symmetric distribution there exists a **unique** area averaged distribution, independent of the direction of the plane used for averaging, the Fourier transform of which differs from the Fourier transform of the radial distribution function by a constant. We also show that the mapping between the area averaged distribution and the radially symmetric distribution function is **invertible**.

We begin with a radially symmetric distribution $g(\mathbf{r}, t) = g(|\mathbf{r}|, t)$. Its Fourier transform is given by

$$g(\boldsymbol{\alpha}, t) = g(|\alpha|, t) = \frac{1}{(2\pi)^{3/2}} \int_r g(\mathbf{r}, t) \exp(i\boldsymbol{\alpha}.r)\, dr.$$

Since $g(|\alpha|, t)$ depends only on $|\alpha|$, we may simplify the above expression by using $\boldsymbol{\alpha} = \alpha_z \mathbf{k}$,

$$g(|\alpha|, t) = \frac{1}{(2\pi)^{3/2}} \int_z \left[\int_x \int_y g(x, y, z, t)\, dx\, dy \right] \exp(i\alpha_z z)\, dz$$

$$= \frac{1}{(2\pi)^{3/2}} \int_z g_a(z, t) \exp(i\alpha_z z)\, dz \qquad [2.1]$$

where

$$g_a(z, t) = \int_x \int_y g(x, y, z, t)\, dx\, dy \qquad [2.2]$$

is the area averaged distribution obtained by averaging the radially symmetric distribution $g(|r|, t)$ over the xy-plane. Since the left-hand side of [2.1] is independent of the orientation of the plane used for averaging, $g_a(z, t)$ is also independent of the orientation of the plane used for averaging. Furthermore, the symmetry of the radially symmetric distribution implies that $g_a(z, t)$ is an even function of z, and hence its Fourier transform is real. The last relation can be simplified further by noting that the expression on the right-hand side is the Fourier transform of $g_a(z, t)$ times $1/(2\pi)$: i.e.

$$g(|\alpha|, t) \equiv \frac{1}{2\pi} g_a(\alpha, t). \qquad [2.3]$$

Therefore, the Fourier transform of the area averaged distribution $g_a(z, t)$, that is obtained from a radially symmetric distribution function using [2.2], is equal to 2π times the Fourier transform of the radial distribution function. This result allows us to go from the Fourier transform of an area averaged distribution to the Fourier transform of the radial distribution, and thus from a one-dimensional area averaged distribution to the corresponding radial distribution. Hence, the mapping [2.2] between the radial distribution function $g(|r|, t)$ and the area averaged one-dimensional function $g_a(z, t)$ is invertible. Therefore, the one-dimensional area averaged distribution $g_z(z, t)$ is equivalent to the radially symmetric distribution function $g(|\mathbf{r}|, t)$. Therefore, the results of diffraction studies are directly relevant to our one-dimensional theory, and a comparison between the results can be made in the Fourier transform space without transforming the data.

3. TWO-VARIABLE AND THREE-VARIABLE THEORIES OF FLUIDIZED SUSPENSIONS

We begin this section with a brief review of one-dimensional **particle phase theories** of three-dimensional fluidized suspensions. In these one-dimensional theories only the effects of variations of fields averaged on the planes perpendicular to flow are modelled. The words "particle phase" mean that the momentum balance for the fluid and solid phases is **decoupled**, and thus it is possible *a priori* to model the effects of fluid on the particles. In this case we get a two-variable, one-dimensional theory of the type proposed by Jackson (1963), Anderson & Jackson (1967), Wallis (1969), Foscolo & Gibilaro (1984, 1987) and Batchelor (1988) for the number density $N(z, t)$ and the particle velocity $u(z, t)$. The number density satisfies the usual conservation law

$$\frac{\partial N}{\partial t} + \frac{\partial (uN)}{\partial z} = 0 \qquad [3.1]$$

where z is in the direction of the fluidizing velocity u_c, and both N and u denote their respective values for the particles whose **centers** are at z, at time t.

In order to close the system with a momentum equation for the particles, we need an estimate of the average drag force acting on a typical particle of the fluidized suspension. Wallis, Foscolo and Gibilaro, and Batchelor have proposed essentially similar forms for the average drag. The main idea used in obtaining the functional form of the average drag is that the drag acting on a particle in a **uniformly** fluidized state **exactly** balances the buoyant weight of the particle. However, these drag laws neglect the fact that in a real fluidized suspension the spatial distribution of particles is nonuniform, and thus the particles are constantly subjected to quadi-random forces. Therefore, the drag law, at best, captures the time average of the actual time dependent quasi-random drag force.

In this paper we will use the following expression proposed by Foscolo & Gibilaro (1987) for the average drag force acting on a single particle

$$F(u, \Phi) = m\tilde{g}\left\{-(1-\Phi) + \left[\frac{u_c - u}{U(0)}\right]^{4.8/n}(1-\Phi)^{-3.8}\right\}. \qquad [3.2]$$

Here m is the mass of a single sphere of radius R,

$$\tilde{g} = \frac{(\rho - \rho_f)g}{\rho}$$

is the reduced gravity, ρ is the density of the sphere, ρ_f is the density of the fluid, $U(\Phi)$ is the steady fall velocity under gravity of a sphere in a uniform dispersion of spheres of solids fraction Φ, $\Phi = \frac{4}{3}\pi R^3 N$, $u_c = u_f(1-\Phi) - u\Phi$ is the fluidization velocity and u_f is the fluid velocity. In order to show that the above expression satisfies the Richardson–Zaki correlation, we note that in a uniform suspension: $F = 0$, $u = 0$, and therefore

$$u_c = U(\Phi) = U(0)(1-\Phi)^n \qquad [3.3]$$

where $U(0)$ is the velocity of one sphere in a pure liquid which can be expressed in terms of the Reynolds number using various empirical correlations, and $n(\mathrm{Re})$ is the Richardson & Zaki exponent; it lies between 4.8 for small Reynolds numbers $\mathrm{Re} = u_c 2R/\nu$ and 2.4 for large Re.

We note that the above expression for the drag law assumes that the drag depends on the **local** solids fraction, defined as $\Phi = \frac{4}{3}\pi R^3 N$. It also assumes that in a uniformly fluidized suspension the particles are uniformly distributed and have zero velocity. But, as we have noted earlier, in a real fluidized bed these two conditions are **never** satisfied. Another problem is that once we have accepted the functional form of the drag law, then it **applies** to all spatial distributions of the solids fraction, including the case where the solids fraction changes at scales **comparable** or **smaller** than the diameter.

The momentum equation of Foscolo & Gibilaro can be expressed as

$$mN\left(\frac{\partial u}{\partial t} + u\frac{\partial u}{\partial z}\right) = NF + K\frac{\partial \Phi}{\partial z} \qquad [3.4]$$

where K is a constant that depends on the parameters of the fluidized suspension. The gradient term proportional to $\partial\Phi/\partial z$ takes into account the contribution of the particle phase pressure. This type of system has also been developed by Batchelor and the gradient term interpreted there in terms of diffusion against the gradient of concentration that causes empty places to fill up as a result of small fluctuations in the particle velocity. This effect is analogous to the effect of Brownian motion in gases. In order to have diffusion against the gradient K must be positive.

Equations [3.1] and [3.4] are then a system of one-dimensional equations in two variables Φ and u. Uniform fluidization with a constant $\Phi = \Phi_0$ and $u = 0$ is a solution of [3.1] and [3.4], but it is Hadamard unstable when the gradient term in [3.4] is neglected (see section 4). The gradient term can regularize this instability and even introduce regions in the space of parameters where the uniform state is stable.

Furthermore, it is easy to show that in this case the criterion for the loss of stability is independent of the wave number of the perturbation, so if the system is unstable at all, it is unstable to long waves as well as to short waves [see Jones & Prosperetti (1985); Prosperetti & Jones (1987) and Prosperetti & Satrape (1989)].

In the remainder of this section we develop a new theory in which the finite size of the particles is accounted for in the drag law. The term based on the gradient of the volume fraction which expresses the particle phase pressure is not included in the present theory. As we shall see, this introduction of the finite size makes it a three-variable theory. We call it a *zeroth order theory* because the gradient terms are not included.

Central to our three-variable theory is a little construction which relates the ensemble averaged number density N, to the fractional area. Consider a plane at $z = z_1$, perpendicular to gravity, as shown in figure 3. Let us consider a square of area $A = L^2$ in this plane with $L \gg R$, so many spheres intersect the plane at z_1. Let x be the distance from the plane z_1. All spheres whose centers are at $|x| \leqslant R$ have a nonzero area of intersection with the plane z_1. Also note that spheres with $|x| \geqslant R$

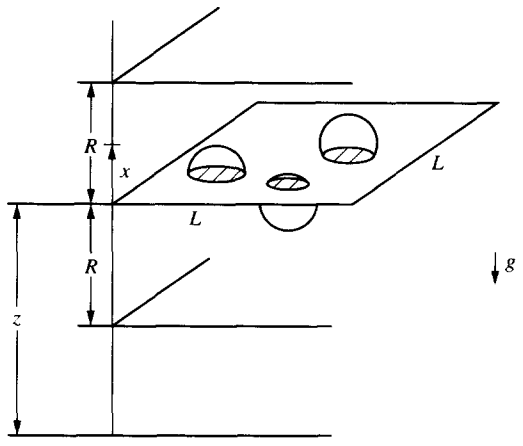

Figure 3. Cross-section of fluidized spheres of radius R in the plane z_1.

do **not** touch the plane z_1. Recall that $N(z_1 + x, t)$ is the number of spheres per unit volume with centers at $z = z_1 + x$, and that the area of intersection of one of these spheres with the plane z_1 is $\pi(R^2 - x^2)$ (see figure 3). The differential number of spheres contained in a rectangular box of height dx, centered at $z = z_1 + x$, is $N(z_1 + x, t)A\,dx$. Hence the total differential area of intersection of the spheres contained in this rectangular box with the plane z_1 is $\pi(R^2 - x^2)N(z_1 + x, t)A\,dx$. Therefore, the area of plane z_1 covered by the particles, $A_s(z_1, t)$, is obtained by summing all of the areas of intersections coming from infinitesimal volumes centered on $x + z_1$ as x varies from $-R$ to R

$$A_s(z_1, t) = \int_{-R}^{R} N(x + z_1, t)\pi(R^2 - x^2)A\,dx. \qquad [3.5]$$

The fractional area of the plane z_1 covered by the particles is, $A_s/A = \phi_a$. It is convenient to substitute $\Phi = \frac{4}{3}\pi R^3 N$ in [3.5], then after dropping the subscript 1 we get

$$\phi_a(z, t) = \int_{-R}^{R} N(x + z_1, t)\pi(R^2 - x^2)\,dx = \frac{3}{4R^3}\int_{-R}^{R} \Phi(x + z, t)(R^2 - x^2)\,dx. \qquad [3.6]$$

From this equation we note that when Φ is independent of x

$$\phi_a(z, t) = \Phi(z, t) = \Phi_0 = \tfrac{4}{3}\pi R^3 N_0 \qquad [3.7]$$

where N_0 is the average number density. Therefore, in this case the area fraction and the solids fraction are equal. This relation holds approximately also when R is small compared to the distance over which N varies significantly. We remind the reader that this is the condition under which the drag law [3.2] is derived.

The next step in the construction of the three-variable theory is to replace the solids fraction Φ in the force law [3.2] with the area fraction ϕ_a, i.e.

$$F(u, \phi_a) = m\tilde{g}\left\{-(1 - \phi_a) + \left[\frac{u_c - u}{U(0)}\right]^{4.8/n}(1 - \phi_a)^{-3.8}\right\}. \qquad [3.8]$$

We could state this as a hypothesis that the average value of the drag force acting on a particle depends on the blocked area normal to the flow direction. Of course, the actual functional form of the drag is expected to be far more complicated, but since at present it is **not** known we will proceed with the understanding that our drag law is only a crude approximation of the actual drag law. However, note that the modified drag law [3.8] reduces to [3.2] in a uniformly fluidized suspension, as can be seen by substituting [3.7] in [3.8]. The same is approximately correct when the wavelength of the disturbance perturbing the uniform state is much larger than the particle diameter (i.e. in the long wave limit, see section 4 for details). Therefore, since the original drag law [3.2] was derived for uniform fluidization and that the two laws are identical in this limit, we are **only** modifying its form in the **regime** where its true form is **not** known. However, we wish to stress that our objective in this paper is only to show that the dispersion relation for a drag law

based on the area fraction has some unique features that are also present in the power spectrums of the real fluidized suspensions. The correct form of the drag law is not the central issue in this paper, and therefore we will only compare qualitatively the forms of the spatial and temporal power spectrums for the theory with that for the experimental data.

The zeroth order three-variable theory for the area fraction based drag law is then given by

$$\frac{\partial \Phi}{\partial t} + \frac{\partial (u\Phi)}{\partial z} = 0, \tag{3.9}$$

$$\phi_a = \frac{3}{4R^3} \int_{-R}^{R} \Phi(x+z, t)(R^2 - x^2)\, dx, \tag{3.10}$$

$$\frac{\partial u}{\partial t} + u\frac{\partial u}{\partial z} = \tilde{g}\left\{-\epsilon + \left[\frac{u_c - u}{U(0)}\right]^{4.8/n} \epsilon^{-3.8}\right\} \tag{3.11}$$

where $\epsilon = 1 - \phi_a$. Obviously uniform fluidization, $u = 0$, $\Phi = \phi_a = \Phi_0$, is a solution of this system of equations.

At this point we want to state how the quantities defined in our three-variable model are to be obtained. We obtain $N(z, t)$ and $u(z, t)$ by ensemble averaging in the manner set down by Joseph & Lundgren (1990). It is necessary to think of ensemble averages rather than volume averages because we shall be looking at fields that vary over the length R of the microstructure. The fractional area ϕ_a is the convolution of the ensemble averaged number density. The main idea of our model is to replace the volume fraction Φ in the force law [3.2] by the area fraction ϕ_a, where the two are related by the simple construction [3.6]. We have constructed our model as a hypothesis which seems reasonable, but at present cannot be proved. However, as we shall see, the results obtained from this theory are in good agreement with the experiment data presented in section 5, as well as with the data obtained from diffraction techniques by Wai, Wignall *et al.* and Ottewill.

In the remainder of this section we obtain some mathematical properties of relation [3.6]. For obtaining these properties we will assume that the number density is in the Fourier transform class because in this case it is easy to integrate the integral in [3.6]. By definition, when N is the Fourier transform class

$$N(x, t) = \frac{1}{2\pi} \int_{-\infty}^{\infty} N(\alpha, t)\exp(i\alpha x)\, d\alpha \tag{3.12}$$

where $N(\alpha, t)$ is the Fourier transform of $N(x, t)$. By substituting this form of the number density in [3.6], we get

$$\phi_a(z, t) = \frac{1}{2} \int_{-R}^{R} \int_{-\infty}^{\infty} N(\beta, t)\exp(i\beta(x+z))(R^2 - x^2)\, d\beta\, dx.$$

By taking the Fourier transform of the above equation, we have

$$\begin{aligned}\phi_a(\alpha, t) &= \int_{-\infty}^{\infty} \phi_a(z, t)\exp(-i\alpha z)\, dz \\ &= \frac{1}{2} \int_{-\infty}^{\infty} \exp(-i\alpha z) \int_{-R}^{R} \int_{-\infty}^{\infty} N(\beta, t)\exp(i\beta(x+z))(R^2 - x^2)\, dx\, d\beta\, dz.\end{aligned}$$

After changing the order of integration in the above, we get

$$\begin{aligned}\phi_a(\alpha, t) &= \frac{1}{2} \int_{-\infty}^{\infty} dz \int_{-\infty}^{\infty} \exp(i\beta z)N(\beta, t)\, d\beta \int_{-R}^{R} \exp(i\beta(x+z))(R^2 - x^2)\, dx \\ &= \frac{2R^3}{3} \int_{-\infty}^{\infty} \Theta(\beta R)\, d\beta \int_{-\infty}^{\infty} \exp(i(\beta - \alpha)z)N(\beta, t)\, dz \\ &= \frac{4\pi R^3}{3} \Theta(\alpha R)N(\alpha, t)\end{aligned} \tag{3.13}$$

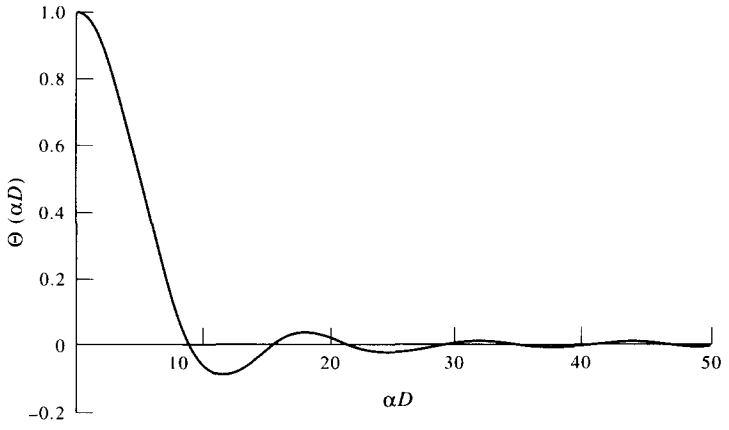

Figure 4. $\Theta(\alpha D)$ is plotted as a function of αD.

where

$$\Theta(\alpha R) = 3\left[\frac{\sin \alpha R}{(\alpha R)^3} - \frac{\cos \alpha R}{(\alpha R)^2}\right] \qquad [3.14]$$

is the blockage function. The graph of $\Theta(2\alpha R)$ vs $2\alpha R$ is shown in figure 4. From [3.13] we conclude that when the number density is in the Fourier transform class then the dimensionless wave numbers, $2\alpha R$, for which $\Theta(\alpha R)$ is zero, are blocked (i.e. are missing) in the spectrum of the area fraction. We will refer to these wave numbers as "blocked wave numbers."

Although, the mathematical implications of relation [3.13] between the area fraction and the number density are obvious, the following ideas are helpful in developing a better intuitive understanding of the geometric constraints imposed on a monodisperse suspension of spherical particles. These ideas are developed in terms of a monochromatic periodic disturbance of wave number α, i.e.

$$N(t, z) = N_0 + N_1(t)\mathrm{Re}[\exp(-i\alpha z)]$$

where N_0 is the average number density, N_1 is the amplitude of the disturbance, and $\mathrm{Re}[\exp(-i\alpha z)]$ is the real part of $\exp(-i\alpha z)$. For N to be physically meaningful $N_0 \geqslant N_1$. After substituting the above expression for N in [3.6] and evaluating the integral, we get

$$\phi_a(z, t) = \tfrac{4}{3}\pi R^3(N_0 + \Theta(\alpha R)N_1(t)\mathrm{Re}[\exp(-i\alpha z)]). \qquad [3.15]$$

From this relation we arrive at the following conclusions:

(1) If for a monochromatic disturbance of wave number α, $\Theta(\alpha R) = 0$, then it is obvious from [3.15] that $\phi_a(z, t) = \frac{4}{3}\pi R^3 N_0 = \text{constant}$. Therefore, for the blocked wave numbers the area fraction is **constant** in space, even though the number density distribution oscillates in space. This raises the following very important question—what effect do these blocked wave numbers have on the number density distribution, and on the overall dynamical behavior of the system?

(2) The fact that $\Theta(\alpha R)$ is a rapidly decaying function of αR (see figure 4) implies that large wave numbers in the area fraction spectrum are **strongly** damped. Therefore, if the average drag acting on the particles depends on the area fraction, then the role played by large wave numbers in the dynamical response is greatly reduced.

(3) Lastly, we note from figure 4 that $\Theta(\alpha R)$ is negative for certain αRs. This implies that for a monochromatic disturbance of wave number α, with $\Theta(\alpha R)$ negative, ϕ_a is smaller than $\frac{4}{3}\pi R^3 N_0$ at places where N is larger than N_0, and *vice versa*. Furthermore, if the drag acting on a particle depends on the area fraction, then the magnitude of the drag is larger than the average drag, at places where $N < N_0$, and *vice versa*. This result is counter intuitive, but can be easily understood if we note that the wavelengths for which $\Theta(\alpha R)$ is negative are smaller than D.

We show next that the area fraction flux $q(z, t)$, passing through the plane z at time t, is also blocked. In order to obtain an expression for the area fraction flux, we note that the net area fraction flux contribution from the particles that are between x and $x + \mathrm{d}x$ is $N(x + z, t)u(x + z, t)\pi(R^2 - x^2)\,\mathrm{d}x$. Therefore, the total flux can be obtained by integrating from $-R$ to R,

$$q(z, t) = \int_{-R}^{R} N(x + z, t)u(x + z, t)\pi(R^2 - x^2)\,\mathrm{d}x. \tag{3.16}$$

Since the convolution in the above relation is same as in [3.6], it is easy to show that the spatial distribution of the flux is also blocked, i.e.

$$q(\alpha, t) = \frac{4\pi R^3}{3}\Theta(\alpha R)(Nu)(\alpha, t)$$

where $(Nu)(\alpha, t)$ is the Fourier transform of the product $N(z, t)\,u(z, t)$, and $q(\alpha, t)$ is the Fourier transform of $q(z, t)$.

For a monochromatic periodic disturbance of wave number α an alternative relation between the area fraction flux and Nu can be obtained by assuming:

$$(Nu)(t, z) = (Nu)_0 + (Nu)_1(t)\mathrm{Re}[\exp(-i\alpha z)].$$

After substituting the above expression for Nu in [3.16] and evaluating the integral, we get

$$q(z, t) = q_0 + \tfrac{4}{3}\pi R^3\Theta(\alpha R)(Nu)_1(t)\mathrm{Re}[\exp(-i\alpha z)] \tag{3.17}$$

where $q_0 = \frac{4}{3}\pi R^3(Nu)_0$ is the average value of the area fraction flux. The above relations allow us to conclude:

(1) For a monochromatic number density flux disturbance of wave number α, with $\Theta(\alpha R) = 0$, the spatial distribution of the area fraction flux is constant, even though the number density flux oscillates in space. Therefore, for blocked wave numbers there is a net transport of the number density, but there is **no** net transport of area fraction.

(2) For a monochromatic disturbance of wave number α, with $\Theta(\alpha R)$ negative, $q(z, t)$ is smaller than the average value of q_0 at places where Nu is larger than $(Nu)_0$, and *vice versa.*

4. STABILITY OF UNIFORM FLUIDIZATION

In order to study the stability of uniform fluidization, we linearize [3.9]–[3.11] around the solution $(u, \Phi, \phi_a) = (0, \Phi_0, \Phi_0)$ and find that the system of perturbed equations, denoted by the subscript 1, is

$$\frac{\partial \Phi_1}{\partial t} + \Phi_0\frac{\partial u_1}{\partial z} = 0, \tag{4.1}$$

$$\phi_1 = -\epsilon_1 = \frac{3}{4R^3}\int_{-R}^{R}\Phi_1(z + x, t)(R^2 - x^2)\,\mathrm{d}x, \tag{4.2}$$

$$\frac{\partial u_1}{\partial t} = -\hat{a}u_1 - \hat{b}\epsilon_1, \tag{4.3}$$

where

$$\hat{a} = \frac{4.8\tilde{g}}{nU(0)}\epsilon_0^{1-n}, \tag{4.4}$$

$$\hat{b} = 4.8\tilde{g}. \tag{4.5}$$

After eliminating ϵ_1 and u_1 from [4.1]–[4.3], we find a single second order equation

$$\frac{\partial^2\Phi_1}{\partial t^2} = -\hat{a}\frac{\partial \Phi_1}{\partial t} - \hat{b}\Phi_0\frac{3}{4R^3}\frac{\partial}{\partial z}\int_{-R}^{R}\Phi_1(z + x, t)(R^2 - x^2)\,\mathrm{d}x. \tag{4.6}$$

The stability of uniform fluidization may be determined by analysis of [4.6] using normal modes

$$\Phi_1 = \hat{\Phi}_1 e^{\sigma t} e^{i\alpha z}. \tag{4.7}$$

We obtain a complex dispersion relation of the form

$$\sigma^2 + \sigma\hat{a} + i\alpha\hat{b}\Phi_0\Theta(\alpha R) = 0, \tag{4.8}$$

where $\Theta(\alpha R)$ is given by [3.14].

We may solve this quadratic equation for

$$\sigma = -\frac{\hat{a}}{2} \pm \frac{\hat{a}}{2}\sqrt{1 - i\Sigma} \tag{4.9}$$

where

$$\Sigma = \frac{4\alpha\hat{b}\Phi_0\Theta(\alpha R)}{\hat{a}^2}. \tag{4.10}$$

We wish to draw the readers attention to the importance of the blockage function $\Theta(\alpha R)$ because when it is zero the growth rate $\mathrm{Re}(\sigma)$ is also zero. We have already listed the zeros of $\Theta(\alpha R)$, i.e. $\alpha = 4.493/R,\ 7.7253/R,\ 10.904/R, \ldots$ Also note that the blockage function approaches zero for large values of α like $1/\alpha^2$, and therefore the growth rate approaches zero also for large wave numbers. These results for the growth rate are not unique to the nonlinear drag law used in this study. In fact, any drag law based on the area fraction which reduces to [4.3] gives rise to the same results. Therefore, the zeros of the dispersion relation cannot be used to check the validity of the drag law. However, the form of the dispersion relation for the area fraction based drag laws is markedly different from that for the number density based drag law because in the former case there is a set of neutrally stable modes which shall be shown to have significantly less power in the saturated state. These features of the area fraction based model are also seen in the experimental data.

We next consider the nature of the instability of the uniform state for two different limits of short waves ($\alpha \to \infty$). In the first limit we have $\alpha R \to 0$ as $\alpha \to \infty$. This corresponds to the classical case in which finite size effects are neglected which can be recovered from our theory when

$$\alpha\Theta(\alpha R) \to \alpha.$$

It then follows from [4.9] and [4.10] that the growth rate

$$\mathrm{re}\ \sigma \to \sqrt{\hat{b}\Phi_0}\sqrt{\alpha}$$

is unbounded for short waves of wavelength $2\pi/\alpha$, $\alpha \to \infty$. In this case the uniform state of fluidization is Hadamard unstable.

On the other hand, if $\alpha R \to \infty$ as $\alpha \to \infty$, then $\alpha\Theta(\alpha R) \to 0$ and $\sigma \to 0$, and the uniform state is unstable, but not Hadamard unstable. We say that finite size effects regularize the Hadamard instability. Furthermore, when $R > 0$ is fixed then at each and every zero of $\alpha\Theta(\alpha R)$ we have

$$\sigma = 0 \text{ or } -\hat{a},$$

otherwise

$$\mathrm{Re}\ \sigma > 0.$$

The graph of re $\sigma(2\alpha R)$ is shown in figure 5. From this graph we conclude that for $R > 0$, however small, uniform fluidization is unstable, but not Hadamard unstable, i.e. the finite size of particles is a regularizer. We also note that there is a blockage of waves of wavelength $2\pi/\alpha$ for $\alpha = 0,\ 4.493/R$, etc. which are neutrally stable and also do not propagate.

Finally, we note that the growth rate is maximum for $\alpha \sim 2.6/R$. By putting this value in [4.10], and using [4.4] and [4.5], we get

$$\Sigma = \Sigma_m = 2.17 n^2 u_c^2 \frac{\Phi_0}{(1-\phi)D\tilde{g}}. \tag{4.11}$$

In section 5 we shall see that Σ_m, which for the linearized theory determines the maximum value of the growth rate, determines the amplitude of the fluctuations for the solution of the nonlinear

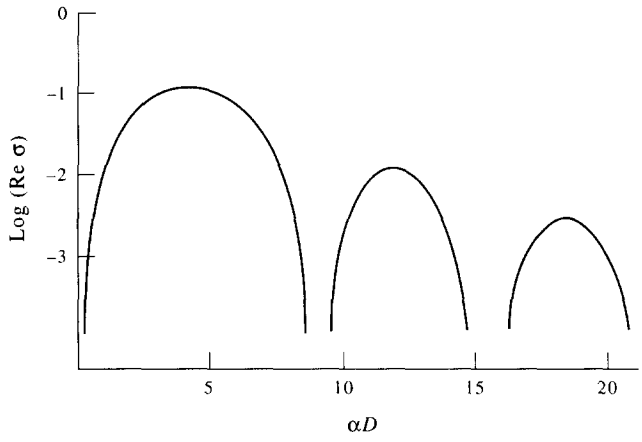

Figure 5. Re $\sigma(\alpha D)$ is plotted as a function of αD.

equations. The physical significance of Σ_m is that it is a ratio of the gravitational and momentum terms.

5. EXPERIMENTS

In this section we briefly describe our experimental results for the area fraction in a two-dimensional bed obtained using the Spin Physics Motion Analysis System (SPMAS) (see Singh (1991) for details). The average area fraction $\phi_a(t, z)$ is the fraction of horizontal plane z covered by the particles at time t. We obtained $\phi_a(t, z)$ at a discrete set of points at constant intervals of z and t. The data obtained were stored in a two-dimensional array

$$\phi_a(i,j) \quad i = 1, \ldots, N, \quad j = 1, \ldots, M,$$

where $\phi_a(i,j) = \phi_a(t_i, z_j)$, $t_i = iT_s$, $z_j = jZ_s$, T_s is the sampling time and Z_s is the sampling distance. The sample mean, $\phi_m = 1/NM\, \Sigma_{ij}\, \phi_a(i,j)$, was removed from $\phi_a(i,j)$. The new zero-mean array thus obtained is for convenience again denoted by $\phi_a(i,j)$. For SPMAS, $M = 239$ but N is essentially unlimited.

For spherical particles listed in table 1 and fluidized in water, we have obtained the data arrays, $\phi_a(i,j)$. The average solids fraction was held approximately constant around 0.25 for three cases listed in table 1. The Reynolds number was changed by changing the density of the fluidized particles. The goal was to analyze the two-dimensional array $\phi_a(i,j)$ for the presence and properties of any spatial or temporal structure, traveling waves or any other distinct statistical structure, and to study how the structures change with Reynolds number.

The temporal autocorrelation for a continuous time ergodic process $\phi_a(t, z)$ is given by

$$r_t(\tau, z) = \lim_{T \to \infty} \frac{1}{T} \int_0^T \phi_a(t + \tau, z)\phi_a(t, z)\, dt \qquad [5.1]$$

where τ is the time shift. The temporal autocorrelation function in the discrete case is given by

$$r_t(n) = \frac{1}{N - n} \sum_{i=1}^{N-n} \phi_a(i,j)\phi_a(i + n, j) \qquad [5.2]$$

Table 1. Diameter, density and Reynolds number for four cases. The Reynolds number is $\mathrm{Re} = u_t D/\nu$ where ν is the kinematic viscosity of water and $u_t = Q/A$ is the superficial velocity, Q is the volume flow rate and A is the area of cross section

Particles	D (cm)	Density (g/cm^3)	Re	ϕ_0
Plastic	0.63	1.12	300	0.24
Glass	0.60	2.46	1650	0.23
Aluminium	0.63	2.70	2000	0.14
Rubber	0.68	4.22	2750	0.22

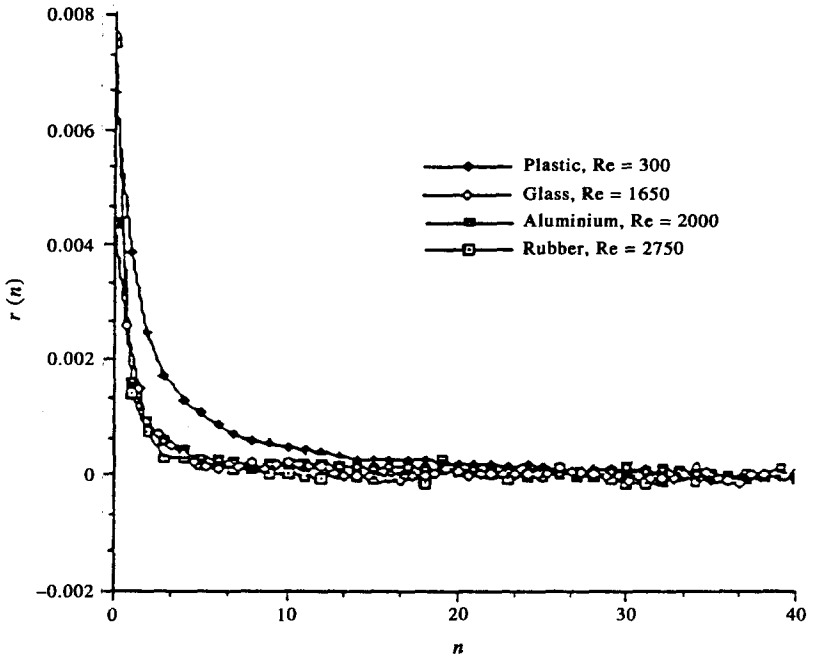

Figure 6. The temporal autocorrelation function as a function of the temporal shift. The temporal sampling time is 0.1 s. The plastic spheres which are fluidized at the smallest Reynolds number (see table 1) have the longest memory. Higher Reynolds numbers are associated with faster decay of the autocorrelation function.

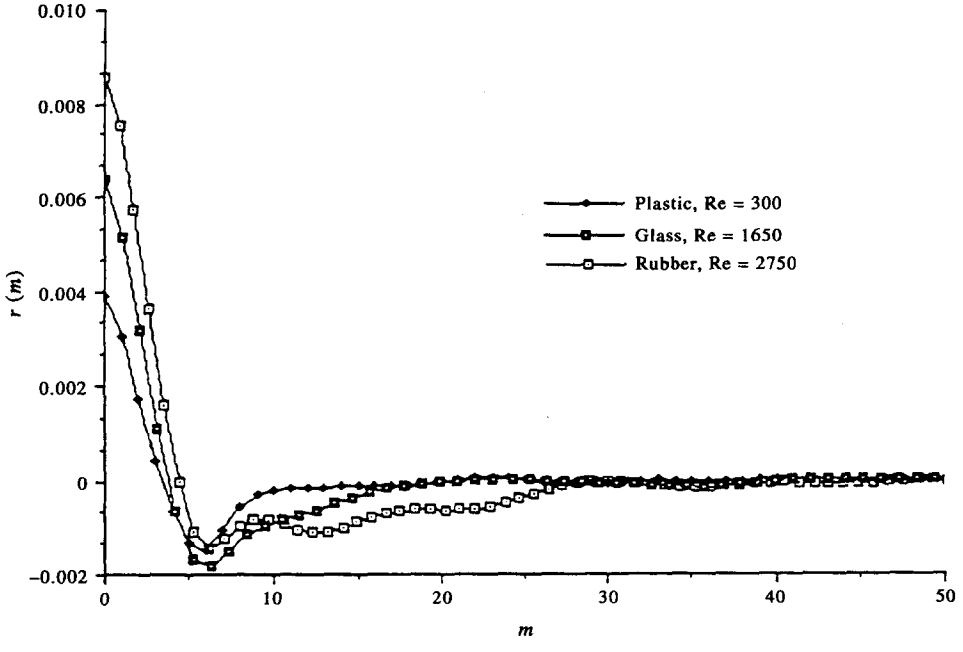

Figure 7. The spatial autocorrelation function as a function of the spatial shift. The sampling distance $Z_s = 0.075$ cm. The variance $r_z(0)$ is a monotonic function of the Reynolds number (see table 1). $r_z(m)$ is minimum for a spatial shift of 0.84 D in dimensional terms. The recovery of $r_z(m)$ to zero is faster when Re is small.

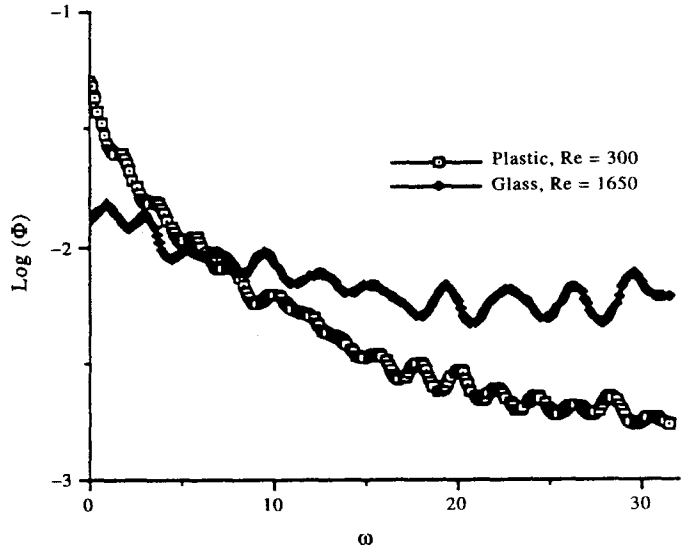

Figure 8. The autoregressive power spectrum as a function of temporal frequency (rad/s). The power spectrum is flatter at higher Re. Flatter spectrum means shorter memory. The apparent fluctuations are due to noise.

where the time shift τ is related to n and the sampling time T_s by $\tau = nT_s$. Similarly, we may compute the spatial autocorrelation function from

$$r_z(t, \zeta) = \lim_{L \to \infty} \frac{1}{L} \int_0^L \phi_a(t, z + \zeta)\phi_a(t, z)\, dz, \qquad [5.3]$$

where ζ is the spatial shift. However, in a practical problem, the spatial length L over which the samples are available is usually too small to give an accurate estimate of the spatial correlation. This problem is easily resolved for a stationary ergodic process with finite temporal memory by averaging over the samples that are obtained after a long enough interval of time. Thus, for an ergodic process the resulting estimate is given by:

$$r_z(\zeta) = \frac{1}{N'} \sum_{i=1}^{N'} \left[\frac{1}{L} \int_0^L \phi_a(t_i, z + \zeta)\phi_a(t_i, z)\, dz \right] \qquad [5.4]$$

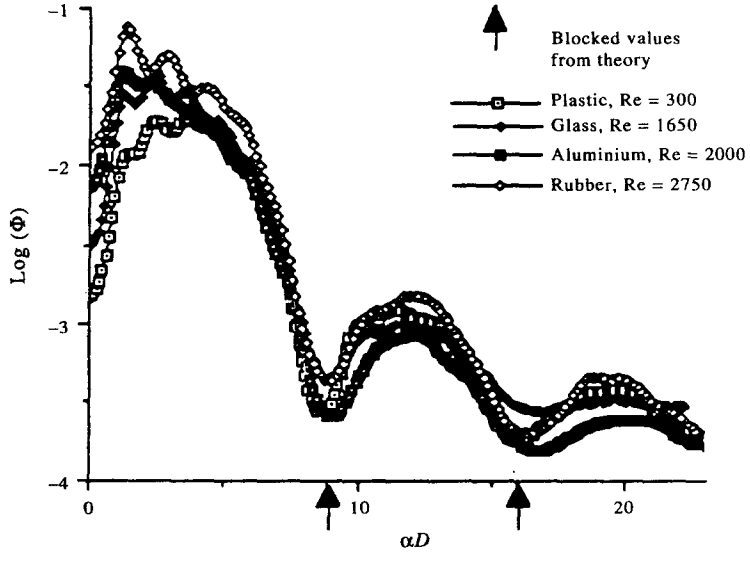

Figure 9. The autoregressive power spectrum for the spatial autocorrelation function [5.5] as a function of nondimensional wave number. The value of αD at the first maximum decreases with increasing Re.

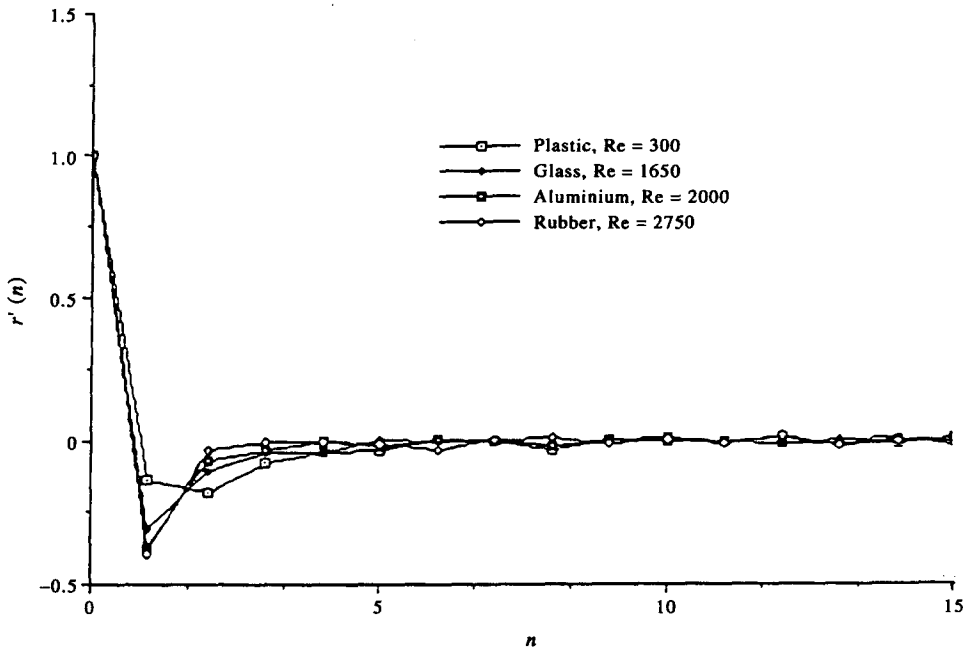

Figure 10. Normalized temporal autocorrelation for the discrete equivalent of the time derivative of the solids fraction. Such changes are uncorrelated for random processes. This figure shows that increases in ϕ are followed on average by decreases; they are negatively correlated.

where i runs over a set of statistically independent samples of ϕ_a. It is straightforward to show that for the discrete case the spatial autocorrelation function is then given by

$$r_z(m) = \frac{1}{N'} \sum_{i=1}^{N'} \left[\frac{1}{M-m} \sum_{j=1}^{M-m} \phi_a(i,j)\phi_a(i,j+m) \right] \qquad [5.5]$$

where i runs over a set of statistically independent spatial distributions, and the spatial shift ζ is related to m and the sampling time Z_s by, $\zeta = mZ_s$.

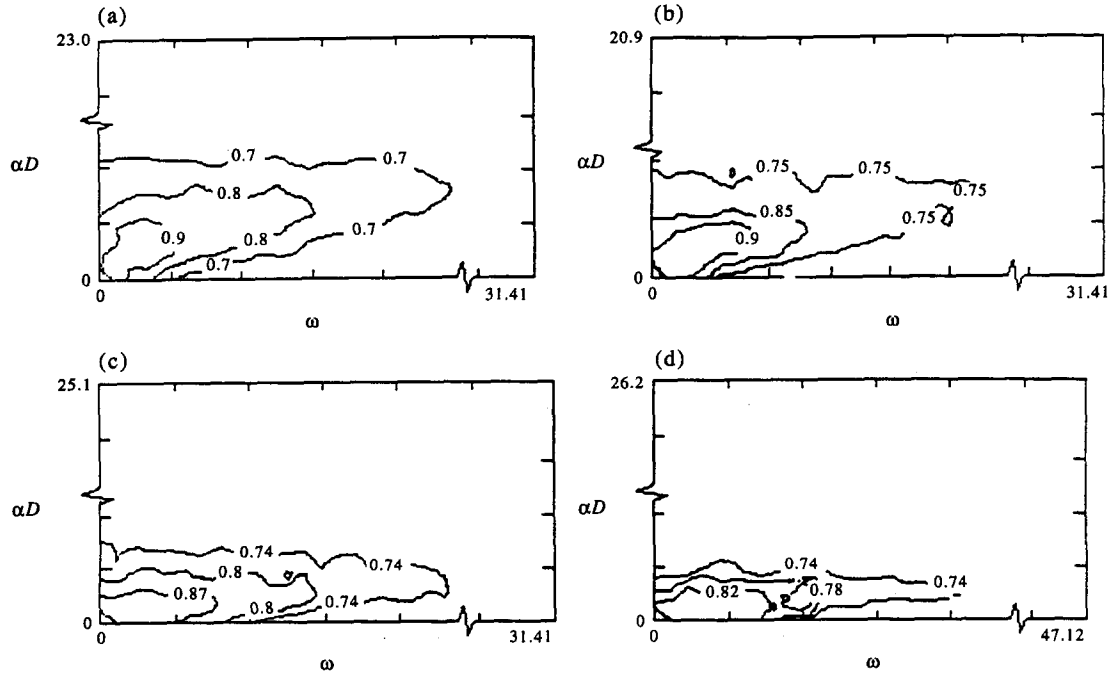

Figure 11. Isovalues of two-dimensional power spectrums are shown as a function of the nondimensional wave number and temporal frequency: (a) plastic, (b) glass, (c) aluminium, (d) rubber (see table 1).

The additional analysis of the data is done in terms of the autoregressive power spectrums. For both the spatial and temporal autocorrelations, we have computed the spectrums by using the Levinson–Durbin recursion [see Roberts & Mullis (1987)].

In figures 6–11 we have presented the results of our data analysis for the area fraction distribution in space and time. Before moving on to a detailed analysis of these figures, we note from figure 6 that for each z the temporal autocorrelation decays monotonically with the temporal shift to zero at an effectively finite time τ_e. Since both the autocorrelation and τ_e are independent of z [see Singh (1991) for a detailed discussion], the fluidized suspension is spatially homogeneous. The power spectrum plots for the temporal autocorrelation functions shown in figure 8 are broad banded; they do not have a dominant frequency. The discretized spatial autocorrelation $r_z(\zeta)$ shown in figure 8 also goes to zero within a finite spatial shift. Therefore, there is no long range correlation in the bed. The power spectrum of the spatial autocorrelation functions shown in figure 9 are also broad banded, but they contain valleys of significantly smaller power. We note that the location of these valleys is the same as of the zeros of the blockage function [3.14]. Therefore, the experimental technique we are using is accurate enough to detect the spectral contents at wavelengths smaller than the diameter.

At this point we briefly note that the results of diffraction studies show that the set of dimensionless minima of the number density spectrum for a fluidized suspension is the same as the net of zeros of the blockage function (see Pusey, Wai, Wignall *et al.* and Ottewill). In these studies, since the scattering techniques are used to detect the spatial structures, the wavelength of the radiation used is comparable to the diameter of the fluidized particles. For example, in Pusey's light scattering study the particle diameter is 0.09 μm, and in Wignall *et al.* the neutron scattering study the particle diameter is 0.1 μm. One advantage of using the diffraction techniques is that the number density spectrum can be obtained directly by using composite particles with core–shell morphology, e.g. when the diffraction diameter of the particles is sufficiently smaller than the mechanical diameter (see Wai, Wignall *et al.* and Ottewill for details). We also note that even though the diameter of the particles used for the neutron and light scattering studies is much smaller than for our study, the set of the dimensionless blocked wave numbers is the same. This result is a consequence of the fact that the only length scale in a fluidized suspension is the particle diameter. Therefore, the results obtained by diffraction studies for very small particles can be compared with our results for much larger particles listed in table 1.

Now we return to a detailed study of the temporal correlation. First, we study the changes in the temporal correlation as the fluidization parameters are varied. From figure 6 we note that the correlation time τ_e, i.e. the time that the temporal autocorrelation function takes to become zero, decreases with increasing Reynolds number. Since τ_e is a measure of the memory of the system, we may conclude that the temporal memory is finite and that it decreases with increasing Reynolds number. However, since the shape of the temporal autocorrelation function remains the same, an observer sitting at a fixed point sees only time scale changes with increasing Re.

The degree of nonuniformity in a fluidized suspension can be quantified by the variance of any suitable variable, such as the number density, area fraction, particle velocity, acceleration, etc. Here we will use the normalized variance of ϕ_a, $\sqrt{r_t(0)}/\phi_0$, as a measure of the magnitude of the fluctuations; when its value is much smaller than one the amplitude of the area fraction fluctuations is much smaller than the average area fraction. On the other hand, when its value is of order one the amplitude of the area fraction fluctuations is comparable to the average value of the area fraction. Obviously, when $\sqrt{r_t(0)}/\phi_0$ is much smaller than one, since the fluctuations of the area fraction (from the average value) are **small** compared to the average value, the spatial distribution of the particles would appear **uniform**. On the other hand, when $\sqrt{r_t(0)}/\phi_0$ is of order one, since the amplitude of the area fraction fluctuations is **comparable** to the average value of the area fraction, the spatial distribution would **not** appear uniform. From figure 6 we note that since $r_t(0)$ increases with increasing Re, the amplitude of the fluctuations grows with increasing Re. Therefore, we conclude that the spatial distribution of particles becomes **less** uniform with increasing Reynolds number. Furthermore, note the autocorrelation and the variance are unique for a given state of fluidized suspension, i.e. the form and shape of the correlations is fixed. In the real space, this is equivalent to saying that the magnitude and the form of the fluctuations are unique to the state of fluidization.

In order to study the statistical behavior of the changes, we define the following differential process

$$\phi_a'(i,j) = \frac{\phi_a(i+1,j) - \phi_a(i,j)}{\phi_0}. \qquad [5.6]$$

Its autocorrelation function

$$r_t'(n) = \frac{1}{N-n} \sum_{i=1}^{N-n} \phi_a'(i,j)\phi_a'(i+n,j), \quad j \text{ fixed}, \qquad [5.7]$$

is obtained in a similar manner, and is shown in figure 10. From this figure, we note that $r_t'(n)$ is independent of j, is negative, and increases monotonically until it becomes zero. As we have already noted in the study of the temporal spectrums, since $r_t'(n)$ goes to zero faster at larger Res, the memory is shorter at larger Res. Also note that $r_t'(n)$ increases in magnitude with increasing Re. Therefore, the magnitude of the fluctuations $r_t(0)$ is larger at larger Res, and since the correlation is negative, the mechanism which counters the fluctuations of the area fraction is stronger at larger Res. Furthermore, since the correlation is nonzero, the fluctuations are not completely random. But, of course, the process has a short temporal memory.

We turn next to a detailed study of the nature of the time averaged spatial autocorrelation (figure 7). For all cases considered the spatial autocorrelation function decreases rapidly and becomes negative. After reaching its maximum negative value it increases and approaches zero uniformly. It is zero for large spatial shifts. The length of the negative spatial memory increases with Reynolds number. This is probably due to the wakes getting bigger with increasing Re. The spatial shift at which the spatial autocorrelation function becomes zero gives us the length scale over which the particle positions are correlated. Therefore, in a fluidized suspension the nearby spheres arrange themselves in a somewhat organized way, but there is no such organization over large distances. Also note that both the length scale of the organized structures and the variance $r_z(m)$ increases with increasing Re. Also, since the power spectrum of the temporal autocorrelation is broad banded, the fluctuations of the voidage from the average value are not periodic in time. If we assume that these fluctuations in the voidage are due to propagating waves then we can safely say that there are no dominant wave numbers.

The spatial spectrum shown in figure 9 is essentially a one-dimensional object, and thus cannot be used to analyze the propagation of structures. To study propagation we use the periodogram method to obtain the two-dimensional power spectrum of $\phi_a(i,j)$

$$F(\omega,\alpha) = \left| \sum_{i=0}^{N-1} \sum_{k=0}^{M-1} \phi_a(i,k) \exp\left(-j\frac{2\pi i\omega}{N}\right) \exp\left(-j\frac{2\pi k\alpha}{M}\right) \right|^2 \qquad [5.8]$$

where $j = \sqrt{-1}$, ω is the temporal frequency and α is the wave number. Again, since M is only 239, the large variance (or the error) of the above estimate is reduced by averaging over several such statistically independent estimates. The two-dimensional power spectrum $F(\omega,\alpha)$ gives a mathematical description of the dispersive properties of the large structures found in the bed. From figure 11 we note that $F(\omega,\alpha)$ is a decreasing function of ω and contains valleys with relatively less power for the blocked wave numbers. In fact, the valleys in the two-dimensional spectrums are so overwhelming that it is difficult to easily visualize any other feature. A detailed study of the spectrum, however, reveals that the blockage exists even in the following one-dimensional distribution: $\omega_m(\alpha)$ where ω_m is the frequency for which $F(\omega,\alpha)$ is maximum for a fixed value of α; thus

$$F(\omega_m,\alpha) = \max_{\omega} F(\omega,\alpha), \qquad [5.9]$$

as can be seen in figure 12 where it is plotted as a function of αD. We note from this plot that for the blocked values of αD the signal peaks at $\omega = 0$, and that for the unblocked αDs it peaks at $\omega \neq 0$. This shows that the propagation velocity of the waves is also related to the blockage function. In particular, the propagation velocity is zero for the blocked wave numbers and it is nonzero for the unblocked wave numbers. This dynamical feature is consistent with the linearized zeroth order theory (see section 4) where we have shown that the waves which correspond to the blocked wave numbers have zero propagation velocity.

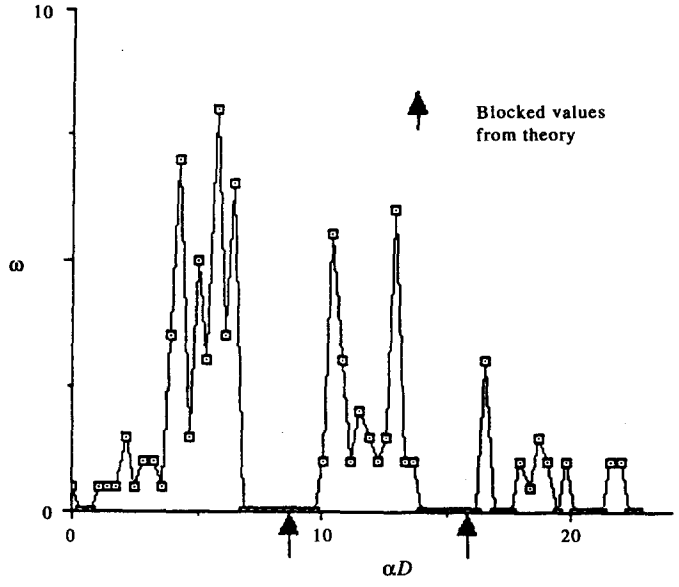

Figure 12. The temporal frequency of the highest power $\max_\omega |F(\omega, \alpha)|$ giving rise to $\omega_m(\alpha D)$ as a function of αD. The highest power is small at the blocked values of αD and $\omega_m(\alpha D) \approx 0$ there.

6. NONLINEAR ANALYSIS

In this section we present numerical solutions of [3.9]–[3.11] obtained by integrating in time for different initial conditions. The Fourier-collocation method is used to spatially discretize the equations. The method assumes that u and N are periodic in space. All results presented in this paper were obtained by solving the equations in a domain, $0 \leqslant z \leqslant 80\,\mathrm{D}$. For the Fourier collocation method u and N are given by

$$u(z_j, t) = \sum_{k=-l}^{l-1} \hat{u}_k(t) e^{ikz_j}$$

$$N(z_j, t) = \sum_{k=-l}^{l-1} \hat{N}_k(t) e^{ikz_j}$$

$$\text{for } j = 0, 1, 2, \ldots, 2l-1, \qquad [6.1]$$

where $2l$ is the number of collocation points. All results presented in this study are for $2l = 512$ or 1024, and have been verified for convergence with increasing l. The collocation points are uniformly distributed within the computational domain. We use a staggered grid for the velocity u and the number density N. The velocities $u(z_j, t)$s are defined as $z_j = 0, \pi/l, \ldots, (2l-1)\pi/l$, and the number densities $N(z_j, t)$s are defined at $z_j = \pi/2l, 3\pi/2l, \ldots, (4l-1)\pi/2l$. A set of nonlinear ordinary differential equations (ODEs) for $u(x_j, t)$ and $N(x_j, t)$ is obtained by substituting the above representations for u and N in [3.9]–[3.11]. These nonlinear ODEs are then discretized using the fifth order implicit Adam–Moulton method. The system of nonlinear equations thus obtained is solved by using the Newton–Raphson method.

In the next few paragraphs we discuss some of the properties of our numerical method. We begin by showing that the use of exponentials as interpolation functions allows us to obtain the integral term in [3.10] exactly, i.e.

$$\phi_u(z_j, t) = 1 - \epsilon = \int_{-R}^{R} N(z + \xi, t)\pi(R^2 - \xi^2)\,\mathrm{d}\xi$$

$$= \int_{-R}^{R} \left[\sum_{k=-l}^{l-1} \hat{N}_k(t) e^{ik(\xi + z_j)} \pi(R^2 - \xi^2) \right] \mathrm{d}\xi$$

$$= \sum_{k=-l}^{l-1} \hat{N}_k(t) e^{ikz_j} \left[\int_{-R}^{R} e^{ik\xi} \pi(R^2 - \xi^2)\,\mathrm{d}\xi \right]$$

$$= \sum_{k=-l}^{l-1} \hat{N}_k(t) e^{ikz_j} \tfrac{4}{3}\pi R^3 \Theta(kR)$$

$$= \tfrac{4}{3}\pi R^3 \sum_{k=-l}^{l-1} [\Theta(kR)\hat{N}_k(t)] e^{ikz_j}, \qquad [6.2]$$

where $\Theta(kR) = 3[\sin kR/(kR)^3 - \cos kR/(kR)^2]$. We note that the sequence $\{\phi_a(z_j, t), = -l, \ldots, l-1\}$ is simply a discrete Fourier transform of the sequence $\{\Theta(kR))\hat{N}_k(t)\}$, and thus the last term in [6.2] can be evaluated by using the Fast Fourier Transform (FFT). We have already noted the properties of the blockage function $\Theta(kR)$, and its effect on the spectrum of the area fraction. In particular, it completely removes the blocked wave numbers from the area fraction, and it significantly diminishes the effect of the wave numbers for which $\Theta(kR)$ is small. Therefore, the dynamical significance of all these wave numbers is significantly reduced because the average force acting on a particle is assumed to depend on ϕ_a.

In order to obtain a numerical scheme which is stable over a long period of time it is necessary that the numerical scheme used conserves $|N|^2$. When global interpolation functions are used to evaluate the derivatives, one of the effects of truncation, i.e. finite l, is the generation of high frequency components (see Canuto *et al.* 1988). Many alternatives are available to overcome this problem. One can apply a low pass filter, do derivative filtering using many different types of filters available and/or add some artificial diffusion to stabilize the numerical scheme. But all these methods suffer from the fact that they modify the equation conserving N in a non-physical way. The method we use in this paper exploits the fact that the grids for N and u are staggered to obtain the correct flux balance. This ensures the stability of the numerical method when integration is carried for a long period of time.

One clear advantage any numerical simulation of the fluid flow has over an actual fluid flow experiment is that numerically one can obtain the Lagrangian quantities with relative ease. In fact, in an experiment it is often impossible to obtain the Lagrangian quantities. The Lagrangian quantities are important for practical reasons because the rates of diffusion and mixing can be estimated from the trajectories of the particles. Thus, for a test particle we will obtain the position, velocity and acceleration as a function of time.

When we integrate [3.9]–[3.11] numerically, we find that the numerical solution changes continuously with time and does not reach any fixed shape or form. One way to overcome this problem is to study it as an initial value problem: i.e. we numerically integrate the system of equations for various initial conditions and parameter values until the power contained in the fluctuations reaches a constant level. We find that the constant power level reached depends on the model parameters, but it is independent of the initial conditions. After the solution has reached the state of constant power level, it fluctuates only slightly from the constant value. We call such solutions **bounded**. By the word "bounded" we mean that the solution is time dependent, but has power level bounded from both above and below.

In order to follow the progress of our numerical solution, we monitor the power contained in the velocity fluctuations:

$$|u(t)|^2 = \frac{1}{2l} \sum_{k=-l}^{l-1} |\hat{u}_k|^2, \qquad [6.3]$$

and the number density fluctuations:

$$|N(t)|^2 = \frac{1}{2l} \sum_{k=-l}^{l-1} |\hat{N}_k|^2 \qquad [6.4]$$

as a function of time. Note that $|N(t)|^2$ and $|u(t)|^2$ are also the variances of the number density and the velocity distributions, respectively. Using our numerical results we would show that the power contained in the velocity and number density fluctuations increases or decreases with time, depending on the **relative** magnitude of its initial value to that of the bounded state for the chosen parameter values. Therefore, even though the power contained or the form of the power spectrum of the bounded solution are not known *a priori*, it is possible to identify the bounded state by monitoring the power contained in the velocity and number density fluctuations.

In order to show that the constant power level of the bounded solution is **independent** of the initial conditions, in figure 13 we have plotted the power contained in the area fraction and velocity

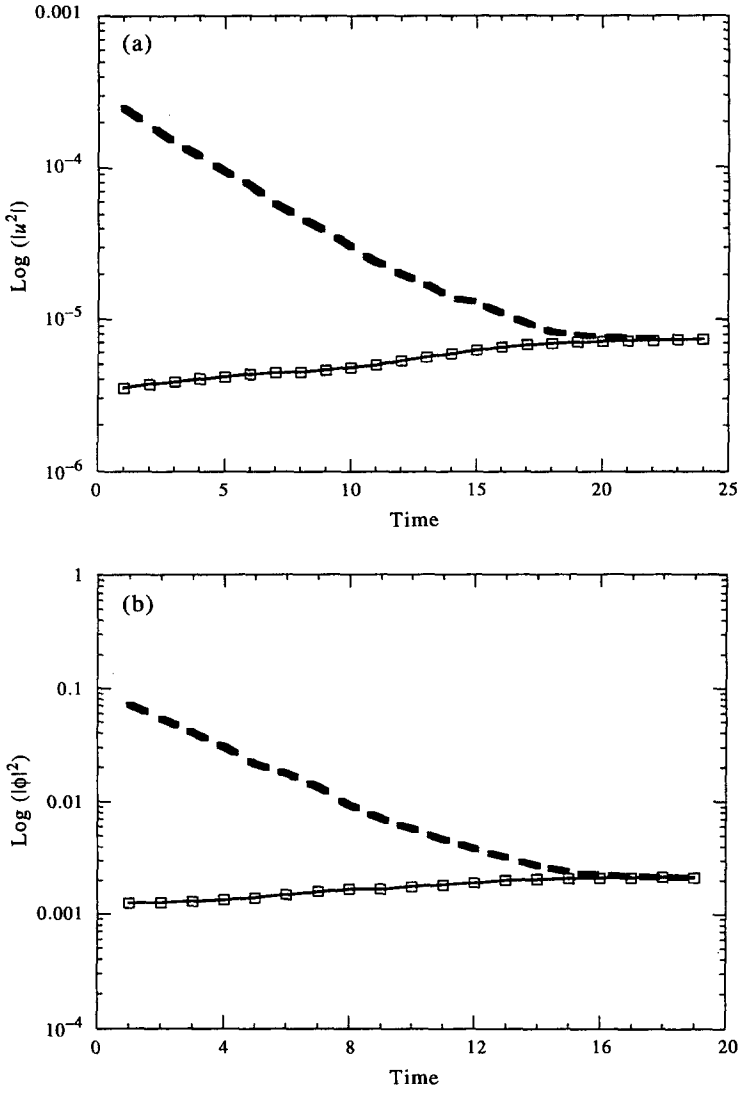

Figure 13. The power contained in the fluctuations of (a) velocity and (b) solids fraction is plotted as a function of time for two different initial conditions.

fluctuations for two different initial conditions, as a function of time. For the first case, the initial power is smaller than that for the bounded state, and for the second case the initial power is larger than that for the bounded state. For both cases the initial spatial distribution for N and u fields is assumed to be random. As expected, for the first case the power contained in the fluctuations grows with time until the nonlinear terms become comparable to the linear terms because the nonlinear terms in this problem are such that the growth of the fluctuations is stopped. The power contained in the fluctuations stops growing when it reaches the level equal to that of the bounded state, and this level is then approximately maintained. On the other hand, in the second case the fluctuations lose power with time until the power is down to the same approximate level as in the first case, and again this level is then approximately maintained. For these two different initial conditions, the power spectrums of the converged bounded solutions, for both the number density and velocity fields, are indistinguishable.

Next, we study the dependence of the bounded solutions on the model parameters. From table 2 we note that for fixed n and Φ_0, the power contained in the fluctuations increases with increasing Σ_m. But, for a given n and Φ_0, there is a maximum value of Σ_m for which a bounded solution exists. When Σ_m is larger than this maximum value the magnitude of the fluctuations of $N(z, t)$ becomes

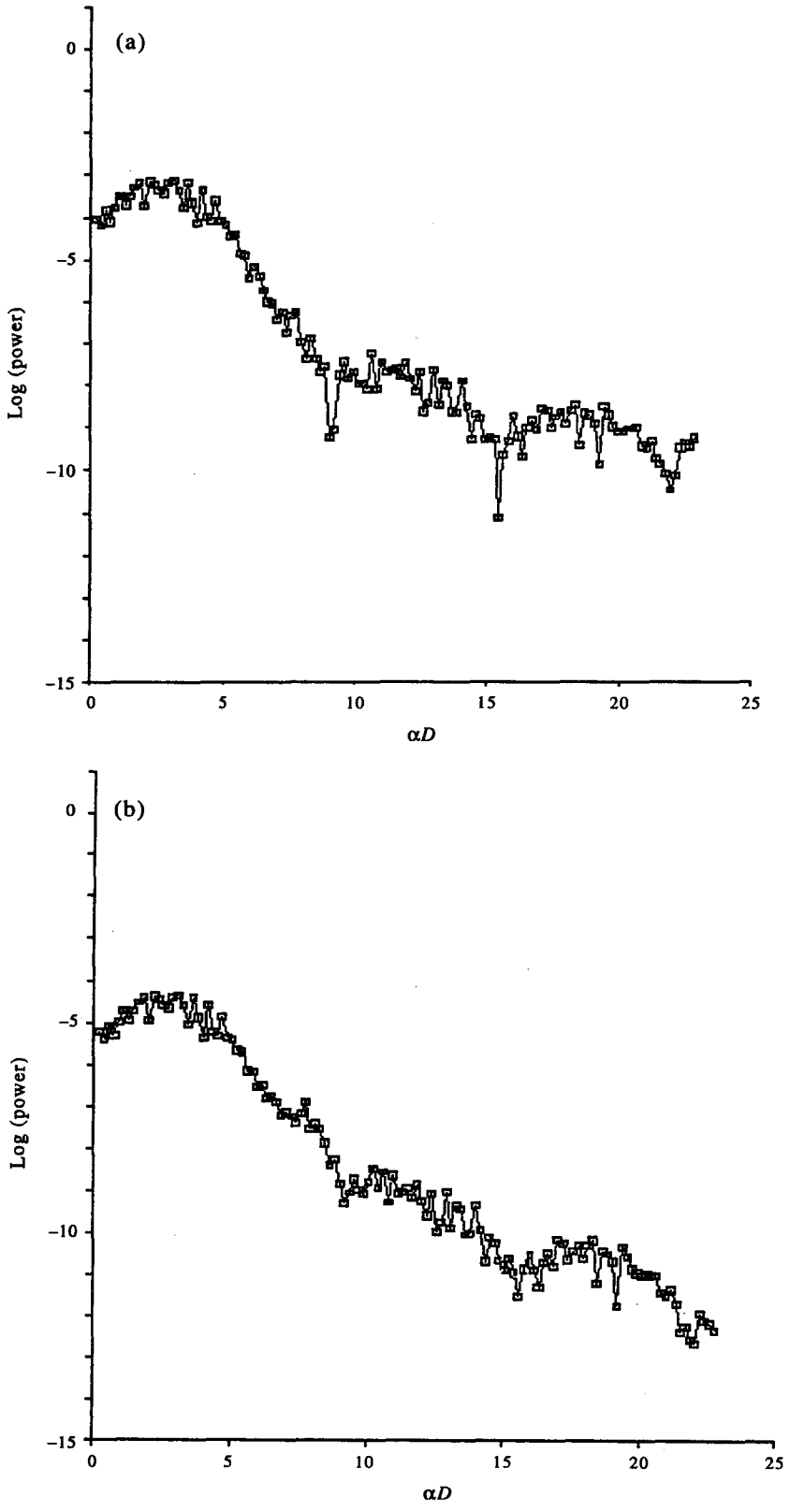

Figure 14. For $\Sigma_m = 0.0094$, $\phi_0 = 0.3$ and $n = 4.8$ the power spectrum of the bounded solution is shown. The blocked modes have very little power: (a) solids fraction, (b) velocity.

comparable to the average of N. This results in the failure of the numerical scheme because there are regions in the domain where $N(z, t)$ is zero (or even negative for numerical simulations). For example, for $n = 4.8$ and $\Phi_0 = 0.3$, the largest value of Σ_m for which a bounded solution exists is 0.93. From the Richardson–Zaki correlation we know that $n = 4.8$ corresponds to small Reynolds numbers. We have picked this particular value of n for our numerical study because the experimental data available for three-dimensional beds; the data by Pusey, Wai, Wignell *et al.* and Ottewill, is for this regime of Reynolds numbers. However, as we have noted earlier, since the experimental data for two- and three-dimensional beds is qualitatively similar, our numerical results can be compared qualitatively with the data presented in section 5 for the two-dimensional bed. But, we must remember that the theory is for unbounded three-dimensional fluidized suspensions.

Although, the bounded solutions have nearly constant power their time evolution as well as their spatial distribution is complicated. Therefore, only the statistical nature of these bounded solutions, in terms of the temporal and spatial power spectrums, is described here. Both spectrums, i.e. the temporal evolution at a fixed point and the spatial distribution for a fixed time, are broad banded [see figures 14(a)–(b)]. From figure 14(a) we note that the spatial power spectrum of the number density contains relatively small power for the blocked wave numbers. This is in general agreement with the experimental results we have presented in section 5, and also with the experimental results of Pusey, Wai, Wignall *et al.* and Ottewill discussed earlier in this paper.

The Lagrangian acceleration for a typical particle and its spectrum are shown in figure 15. Since the spectrum is broad banded, the motion of an individual particle is also a complicated function of time. This agrees well with the observation of VMZ that the particles move on quasi-random paths.

We have noted earlier that for both experiments and numerical simulations, the power contained in the fluctuations and also the amplitude of the fluctuations, depend on the flow parameters. From a practical point of view, we want the power contained in the fluctuations to be as small as possible because then the heat and mass transfer rates between the fluid and the particles are maximum. In a real fluidized suspension, the judgement whether or not the fluctuations are sufficiently small is usually arrived at by looking at the spatial uniformity of the particles and their motion. Therefore, it is important to compare the statistical nature of the fluctuations for a real fluidized suspension with that for the model. We have already seen that the forms of spatial and temporal power spectrums are simlar for the suspensions and the model. Now we note that for both the suspensions and the model, it is possible to control the amplitude of the fluctuations by controlling the parameters. In particular, when Σ_m is smaller than one, the area fraction fluctuations are small compared to its average value. In experiments, the magnitude of the fluctuations increases with increasing flow rate which in turn is proportional to Σ_m (or Re, see section 5). Therefore, when Σ_m is small, the spatial distribution appears uniform because the uniform state dominates, see figure 16. On the other hand, when Σ_m is of order one but smaller than one, the area fraction fluctuations are comparable to the average area fraction in the bed. In this case the spatial distribution does not appear uniform. Furthermore, when Σ_m is larger than one, then the fluctuations are large enough to produce regions in the domain where the area fraction is very small (or even negative for numerical simulations). However, the numerical method failed in this regime. Therefore, we may conclude that as the parameter Σ_m is increased, the spatial distribution of the particles becomes less uniform as the magnitude of the fluctuations increases (see table 2). This allows us to propose the criterion that when

$$\Sigma_m < 1 \qquad [6.5]$$

then the spatial distribution of the particles is sufficiently uniform. That is, there are no regions in the domain where the number density N is too small or too large.

It is interesting to compare the above criterion with the criteria of Batchelor, and Foscolo & Gibilaro for predicting the stability of the fluidized suspensions. We note that their criteria are based on linear stability analysis. Here we will compare our criterion only with the Foscolo &

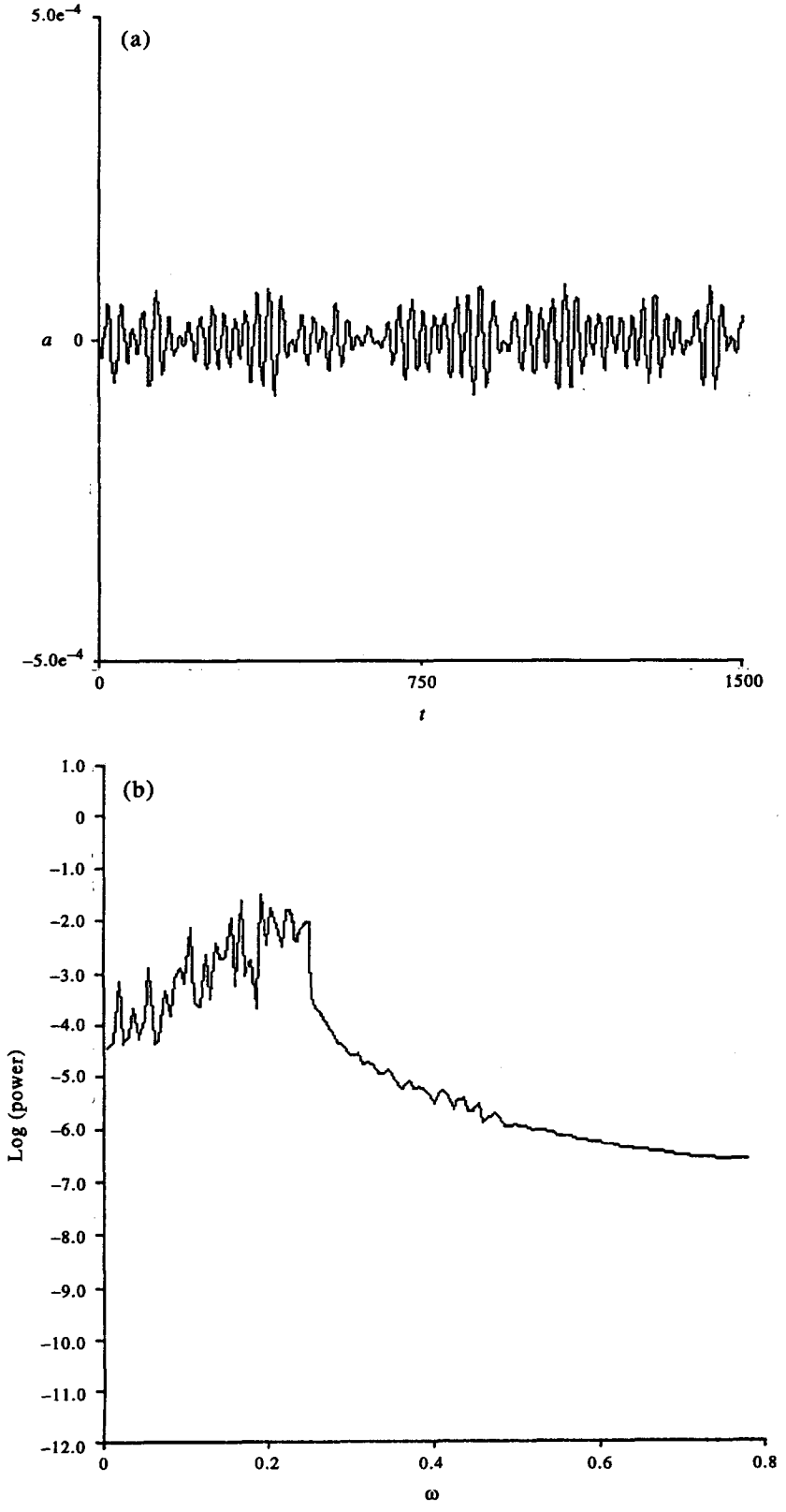

Figure 15. The Lagrangian acceleration, $\Sigma_m = 0.0094$, $\phi_0 = 0.3$ and $n = 4.8$: (a) plotted as a function of time, (b) the power spectrum. The power spectrum is broad banded, hence the particle motion is chaotic.

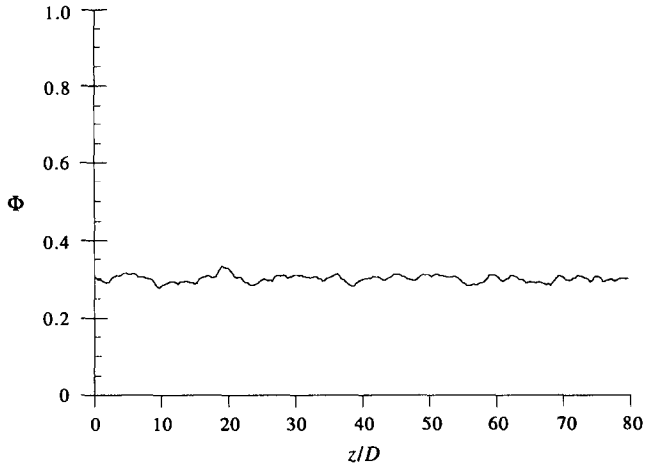

Figure 16. For $\Sigma_m = 0.0094$, $\Phi_0 = 0.3$ and $n = 4.8$, the area fraction for a bounded solution is shown as a function of z. Since $\Phi_0 \gg \max(\phi - \Phi_0)$, the spatial distribution appears uniform.

Gibilaro theory because some of the parameters in Batchelor's theory are not known. In our notation the Foscolo–Gibilaro stability criterion states that a fluidized suspension is unstable if

$$2.6\sqrt{\frac{\rho_p}{\rho_p - \rho_f}}\frac{u_t}{\sqrt{gD}} n\phi^{0.5}(1-\phi)^{n-1} < 1.0 \qquad [6.6]$$

They have used this criterion with some success to predict the onset of bubbling (i.e. a form of instability where the fluctuations from the uniform state are so large that holes, with no particles, appear in the bed). The left-hand side of the above inequality is closely related to Σ_m; thus it is possible to write their criterion in terms of Σ_m as

$$\sqrt{\Sigma_m} < 1.73. \qquad [6.7]$$

Therefore, the Foscolo–Gibilaro criterion predicts instability when $\sqrt{\Sigma_m}$ is larger than 1.73. This agrees well with criterion [6.5] for the nonlinear zeroth order theory. The similarity between the two criteria is apparent, but the two theories are completely different from a mathematical point of view. Specifically, the nonlinear solution predicts instability when the spatial distribution of the particles becomes so uneven that holes with no particles appear in the domain (as is also the case in experiments). On the other hand, the Foscolo–Gibilaro criterion is derived from a linear theory which predicts instability when the kinematic wave speed becomes larger than the dynamic wave speed.

7. CONCLUSIONS

The linear stability analysis of the zeroth order theory shows that uniform fluidization is unstable even when the force acting on a particle is assumed to depend on the area fraction. However, it is not Hadamard unstable, and there is a discrete set of blocked wave numbers for which the growth rate is zero. The numerical simulation of the nonlinear zeroth order theory shows that there are

Table 2. For $\phi_0 = 0.3$ and $n = 4.8$ the power contained in the fluctuations of the area fraction and the velocity, and the maximum area fraction fluctuation are shown for the bounded solutions obtained for five different values of Σ_m

Σ_m	$\frac{\phi_{\max}}{\phi_0}$	$\lvert\phi\rvert^2$	$\lvert u\rvert^2$
0.748	0.860	0.0116	3.3×10^{-3}
0.337	0.597	0.0056	8.0×10^{-4}
0.0958	0.261	0.00062	2.3×10^{-5}
0.0374	0.119	0.000096	1.38×10^{-6}
0.0094	0.031	0.000010	1.46×10^{-8}

time dependent bounded solutions with nearly constant power when $\Sigma_m < 1$. These results are consistent with experimental results for two- and three-dimensional beds where one finds that there are always some fluctuations in the area fraction and number density distributions, and that the amplitude of the fluctuations increases with increasing flow rate (or Σ_m). In fact, it is possible to measure the magnitude, as well as the statistical nature of the fluctuations, as a function the parameters. The statistical nature of the fluctuations is described in terms of the temporal and spatial correlations, and their spectra. The spatial spectrum contains all wavelengths, including wavelengths that are an order of magnitude smaller than the particle diameter. In fact, the maximum of the power spectrum is at a wavelength that is comparable to the particle diameter, and wavelengths smaller than the diameter contain a **significant** portion of the total energy contained in the fluctuations. Therefore, any theory that attempts to describe the nature of fluctuations, must not only allow for wavelengths smaller than the diameter, but also predict their dynamical behavior correctly. This is, at least partially, accomplished in the present zeroth order theory because it allows all wavelengths to grow, and also correctly predicts the qualitative form of the spatial power spectrum, including blockage.

We also wish to note that there is no evidence of stable uniform fluidization, neither in the two-dimensional fluidized suspensions reported by VMZ and here, or in three-dimensional fluidized suspensions of Pusey, Wai, Wignall *et al.* and Ottewill. Nor is there any indication of Hadamard instability.

We conclude by making the following additional observations:

- For a monodisperse suspension of spherical particles, if the number density is in the Fourier transform class, then the geometric relation [3.6] can be used to show that the Fourier transform of the area fraction contains blockage (see equation [3.13]). This equation also shows that if a particular wave number is **missing** in the number density spectrum, or contains very **small** power, then the **same** is true for the area fraction spectrum. The opposite is also true, except when the blockage function is small.
- Both, the experimental data and the results obtained numerically for the zeroth order theory show that the fluctuations have a unique autocorrelation. The temporal autocorrelation is a monotonically decreasing function of the temporal shift, and the spatial correlation decreases to zero for a unique value of the spatial shift which decreases with increasing Reynolds number. The variance (or the magnitude) of the fluctuations at a point increases with increasing Reynolds number.
- The criterion $\Sigma_m < 1$ which we have found for numerical solutions with bounded power is similar to the Foscolo–Gibilaro criterion for bubbly beds which they have obtained by linear stability analysis of uniform fluidization.

Acknowledgements—This research was supported under grants from the National Science Foundation, the US Army Research Office, Mathematics, the Department of Energy, AHPCRC and the Supercomputer Institute of the University of Minnesota.

REFERENCES

ANDERSON, T. B. & JACKSON, R. 1969 A fluid mechanical description of fluidized beds. *Ind. Engng Chem. Fundam.* **8,** 137–144.

BATCHELOR, G. K. 1988 A new theory of the instability of a uniform fluidized bed. *J. Fluid Mech.* **193,** 75–110.

CANUTO, C., HUSSAINI, M. Y., QUARTERONI, A. & ZANG, T. A. 1988 *Spectral Methods in Fluid Dynamics.* Springer, Berlin.

FORTES, A., JOSEPH, D. D. & LUNDGREN, T. 1987 Nonlinear mechanics of fluidization of beds of spherical particles. *J. Fluid Mech.* **177,** 467–483.

FOSCOLO, P. V. & GIBILARO, L. G. 1984 A fully predictive criterion for transition between particulate and aggregate fluidization. *Chem. Engng Sci.* **39,** 1667–1674.

FOSCOLO, P. V. & GIBILARO, L. G. 1987 Fluid dynamic stability of fluidized suspensions. The particle bed model. *Chem. Engng Sci.* **42,** 1489–1500.

GARSIDE, J. & AL-DIBOUNI, M. 1973 Behaviour of liquid fluidized beds containing a wide size distribution of solids. *Fluidization and its Applications*, pp. 53–62. Toulouse.

JACKSON, R. 1963 The mechanics of fluidized beds: Part I: The stability of the state of uniform fluidization. *Trans. Instn Chem. Engrs* **41,** 13–21.

JONES, A. V. & PROSPERETTI, A. 1985 On the suitability of first-order differential models for two-phase flow prediction. *Int. J. Multiphase Flow* **11,** 133–148.

JOSEPH, D. D. & LUNDGREN, T. S. 1990 Ensemble averaged and mixture theory equations for incompressible fluid–particle suspensions. *Int. J. Multiphase Flow* **16,** 35–42.

JOSEPH, D. D., FORTES, A., LUNDGREN, T. & SINGH, P. 1987 Nonlinear mechanics of fluidization of beds of spheres, cylinders and disks in water. *Advances in Multiphase Flow and Related Problems* (Edited by PAPANICOLAU, G.), pp. 101–122. SIAM.

OTTEWILL, R. H. 1991 Small-angle neutron scattering from colloidal particles. *J. Appl. Cryst* **24,** 436–443.

PROSPERETTI, A. & JONES, A. V. 1987 The linear stability of general two-phase flows models—II. *Int. J. Multiphase Flow* **13,** 161–171.

PROSPERETTI, A. & SATRAPE, J. V. 1989 Two phase flows in fluidized beds, sedimentation and granular flows. *IMA Volumes in Mathematics and its Applications 26*, pp. 98–117. Springer, Berlin.

PUSEY, P. N. 1978 *J. Phys. A: Math. Gen* **11,** 119.

RICHARDSON, J. F. & ZAKI, W. N. 1954 Sedimentation and fluidization: Part I. *Trans. Instn Chem. Engrs* **32,** 35–53.

ROBERTS, R. A. & MULLIS, C. T. 1987 *Digital Signal Processing*, Addison–Wesley, Mass.

SINGH, P. 1991 Ph.D. Thesis, University of Minnesota.

SINGH, P. & JOSEPH, D. D. 1990 One-dimensional, particle bed models of fluidized suspensions, two phase flows in fluidized beds, sedimentation and granular flows. *IMA Volumes in Mathematics and its Applications 26*, pp. 130, 149. Springer, Berlin.

SINGH, P. & JOSEPH, D. D. 1991 Finite size effects in a fluidized beds, *Am. Soc. Mech. Engrs*, 77–86.

SINGH, P., CAUSSIGNAC, P., FORTES, A., JOSEPH, D. D. & LUNDGREN, T. 1989 Stability of periodic arrays of cylinders across the stream by direct simulation. *J. Fluid Mech.* **205,** 553–571.

VOLPICELLI, G., MASSIMILLA, L. & ZENZ F. A. 1966 Non-homogenaties in solid–liquid fluidization. *Chem. Engng Symp. Series* **67,** 62, 42–50.

WIGNALL, G. D., RAMAKRISHANAN, V. R., LINNEN, M. A., KLEIN, A., SPERLING, L. H., WAI, M. P., GELMAN, R. A., FATICA, M. G., HOERL, R. H., FISHER, L. W., MELPOLDER, S. M. & O'REILLY, J. M. 1990 The morphology of emulsion polymerized latex particles. *Mol. Cryst. Liq. Cryst.* **180A,** 25–39.

WAI, M. P., GELMAN, R. A., FATICA, M. G., HOERL, R. H. & WIGNALL, G. D. 1987 Small-angle neutron scattering study on the morphology of seeded emulsion-polymerized latex particles. *Polymer* **28,** 918–922.

WALLIS, G. B. 1969 *One-Dimensional Two-Phase Flow*. McGraw–Hill, New York.